[Review Paper]

X-ray Absorption Spectroscopic Characterization of Solid Acid-base Catalysts

Takashi YAMAMOTO*

Dept. of Mathematical and Material Sciences, The University of Tokushima, Minamijyosanjima-cho 1-1, Tokushima 770-8502, JAPAN

(Received September 10, 2014)

Recent X-ray absorption spectroscopic studies of solid acid-base catalysts were reviewed, which have been carried out to investigate the effects of lanthanum-ion addition to alumina for improving the thermal stability, acidity generation mechanism of siliceous mesoporous silica, or state of tungsten oxide species in WO_x–ZrO_2 strong solid acid. Remarks on EXAFS analytical procedures were also discussed about possibility of coexistence of multiple phases, mismatch between radial distribution functions and Fourier transforms of EXAFS, and effects of multiple excitations in an X-ray absorption spectrum.

Keywords

XAFS, Solid acid-base catalyst, Data reduction, Lanthanum oxide–alumina, Tungsten oxide–zirconia, Mesoporous silica

1. Introduction

Since Sayers, Stern and Lytle have developed modern theory of X-ray absorption spectroscopy and Fourier transformation techniques were developed in the early 1970's[1),2)], since when X-ray absorption spectroscopy has been widely utilized as a powerful tool to investigate the chemical states and electronic structure of target elements in many research fields. Further development of the theory, X-ray absorption spectroscopy equipment and facilities, recording techniques, and programs for data reduction has also noticeable. Nowadays, X-ray absorption fine structure (XAFS) spectroscopy including both X-ray absorption near edge structure (XANES) and extended X-ray absorption fine structure (EXAFS) spectroscopy are regarded as conventional characterization techniques, especially in catalyst research[3)~6)]. This review describes our recent XAFS studies of solid acid-base catalysts and discusses EXAFS analysis.

2. Analysis of Solid Acid-base Catalysts

2. 1. Lanthanum-ion Modified Al_2O_3[7),8)]

Aluminas are widely utilized for industrial catalyst supports, and γ-Al_2O_3 is a typical acid catalyst, especially for dehydration due to its Lewis acidity[9)]. The phase transformation of γ-Al_2O_3 to the α-phase and decrease of its surface area, so-called sintering, are serious problems for alumina-based catalysts without deactivation, especially in high temperature usage and in the presence of H_2O vapor, such as in automobile or combustion catalysts. Addition of La-ion to alumina-based catalysts is widely used to enhance the thermal stability of the supports. Many studies have investigated the states of promoted La species and the effects against sintering, and many hypotheses about the mechanisms of La-addition have been proposed[10)~15)].

We prepared LaO_x/Al_2O_3 with different loadings and thermal treatment procedures at temperatures of 773-1423 K, and confirmed that La addition to Al_2O_3 suppresses sintering even at a low concentration of 0.1 mmol La g$(Al_2O_3)^{-1}$ (1.6 wt% as La_2O_3, 0.36 La atom nm^{-2}) (**Fig. 1**)[8)], as reported previously[10),16)~18)].

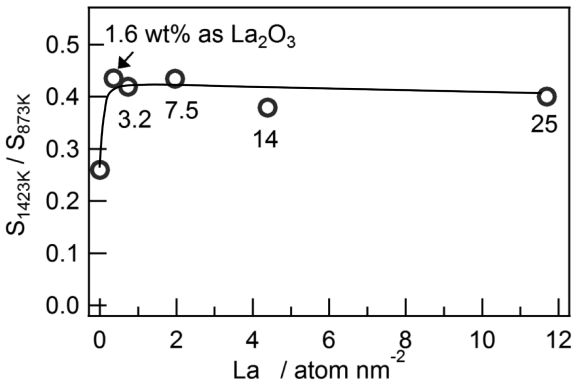

$S_{1423\,K}$ and $S_{873\,K}$ are surface areas calcined at 1423 K and 873 K for 3 h, respectively.

Fig. 1 Dependence of La Concentration in γ-Al_2O_3 on Improvement of the Thermal Stability

DOI: dx.doi.org/10.1627/jpi.57.261

* E-mail: takashi-yamamoto.ias@tokushima-u.ac.jp

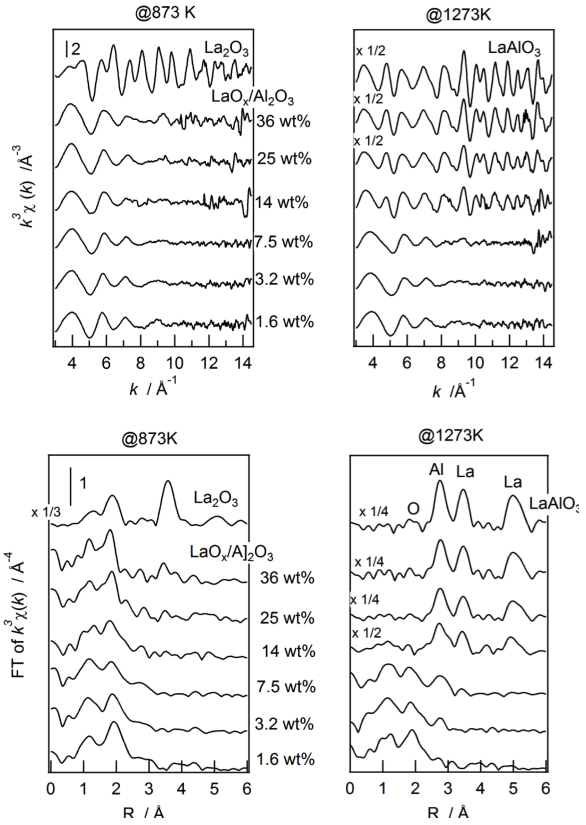

Fig. 2 La K-edge EXAFS Spectra and Fourier Transforms of LaO_x/Al_2O_3 Calcined at 873 K or 1273 K

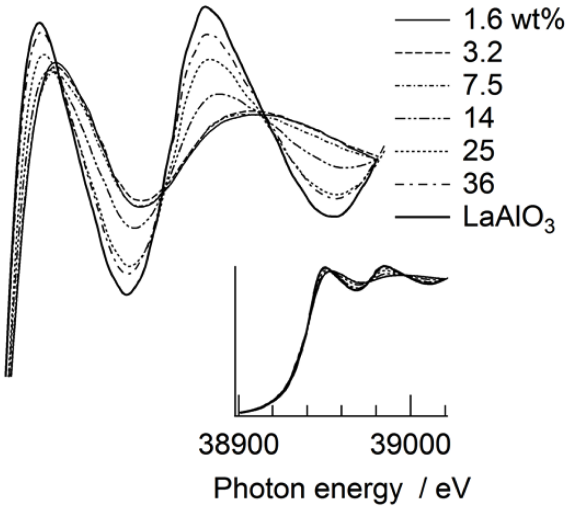

Fig. 3 Series of La K-edge XANES Spectra of LaO_x/Al_2O_3 Calcined at 1273 K with Different Loadings

To clarify the effects of La-ion addition in the suppression of sintering, we investigated the local structure of doped lanthanum species on γ-Al_2O_3 with different loadings and treatment temperatures using La K-edge XAFS, as well as the surface acid-base properties[8].

XRD characterization revealed that no crystalline phases related to lanthanum compounds were confirmed for 1.6-25 wt% LaO_x/Al_2O_3 calcined at 873 K, whereas $LaAlO_3$ phase was detected on LaO_x/Al_2O_3 calcined at 1273 K at loadings of more than 14 wt%. **Figure 2** shows the La K-edge EXAFS spectra of LaO_x/γ-Al_2O_3 with different loadings calcined at 873 K or 1273 K. EXAFS oscillations at calcination temperature of 873 K were negligible in the higher k-region above 8 Å^{-1} (1 Å $= 10^{-10}$ m) , and the radial structure functions (RSFs) did not show a second coordination sphere above 3 Å. After calcination at 1273 K, EXAFS spectra of LaO_x/Al_2O_3 with loadings above 14 wt% and their RSFs showed drastically changed configuration which resembled that of $LaAlO_3$ perovskite. Peaks at 2.8 Å and 3.4 Å in the RSFs (radial sructure functions) were assigned to La–Al and La–La pairs in $LaAlO_3$. In contrast, spectral configurations with low loadings of 1.6-3.2 wt% remained unchanged after calcination, as these loadings were enough to improve thermal stability as shown in **Fig. 1**. XRD analysis did not detect crystalline $LaAlO_3$ phase on 7.5 wt% LaO_x/Al_2O_3 calcined at 1273 K, but the RSF showed small but distinct peaks thought to be La–Al and La–La pairs. These findings show that small amounts of La species are present as $LaAlO_3$, and large amounts of residual species are present as highly dispersed forms and/or in the amorphous state.

The phase transformation of supported lanthanum species caused by thermal treatment can be confirmed by XANES spectra more clearly and quantitatively. Spectral configurations of XANES spectra for 1.6 wt% and 3.2 wt% LaO_x/Al_2O_3 remained unchanged after calcination at 1273 K, but drastically changed to resemble $LaAlO_3$ at higher loadings. **Figure 3** shows the XANES spectra of LaO_x/Al_2O_3 calcined at 1273 K. The spectral features changed gradually after thermal treatment at 1273 K with various loadings. The series of XANES spectra possessed some isosbestic points, so we tried to reproduce all spectra with two standard spectra, of crystalline $LaAlO_3$, and of isolated La species on Al_2O_3. The standard spectrum adopted for isolated La species was that of 1.6 wt% LaO_x/Al_2O_3 treated at 873 K. The convolution analysis could be successfully done for all spectra as shown in **Fig. 4**, for example. The evaluated fractions of the $LaAlO_3$ phase are shown in **Fig. 5**. We proposed that only aggregated La species on Al_2O_3 were transformed to the $LaAlO_3$ binary oxide phase by thermal treatment at 1273 K and isolated La species retained the original oxide-like structure after thermal treatment, as in the case of the CuO_x/Al_2O_3 system[19]. The estimated fractions of $LaAlO_3$ species directly indicate the ratio of aggregates to all La species on Al_2O_3. The fraction of aggregated La species increased with higher loadings, and the threshold for aggregation was 0.5 mmol La g$(Al_2O_3)^{-1}$ (7.5 wt% as La_2O_3). It has been reported by several

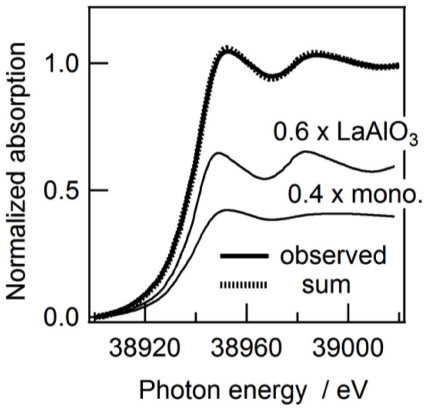

Fig. 4 Simulated La K-edge XANES Spectra of 14 wt% LaO_x/Al_2O_3 with $LaAlO_3$ and Isolated LaO_x Species on Al_2O_3

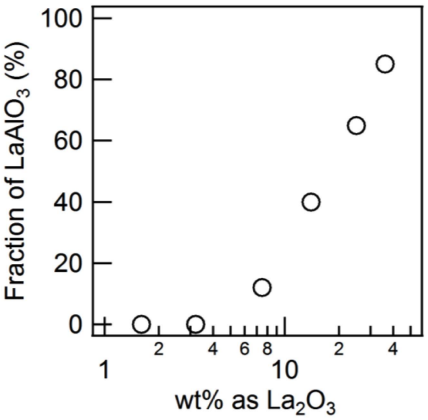

Fig. 5 Estimated Fraction of $LaAlO_3$ on LaO_x/Al_2O_3 Calcined at 1273 K by La K-edge XANES Spectrometry

research groups that only a small amount of La doping (*ca.* 1 mol%) is sufficient for suppression of sintering [16)~18)]. We could confirm that $LaAlO_3$ perovskite phase did not form at lower loadings, indicating that formation of $LaAlO_3$ on the surface layer of Al_2O_3 is not essential to prevent sintering.

It is well known that surface area reduction will proceed much more drastically in the presence of water vapor than in the dry state. Hydrolysis of Al–O–Al linkages to form hydroxyl groups and dehydroxylation might occur repeatedly and rapidly in the presence of water vapor at higher temperatures, leading to such remarkable reduction of surface area. Based on other spectroscopic studies of the acid-base properties of LaO_x/Al_2O_3 and the present catalyses, we confirmed that addition of La atom to γ-Al_2O_3 poisoned the strong Lewis acid sites on γ-Al_2O_3, and converts them to new Lewis acid sites with medium strength, and acted similarly on other types of LnO_x/Al_2O_3 catalysts[20)]. Finally, we proposed a new concept that the mechanism of La addition to enhance the thermal stability of γ-Al_2O_3 is to titrate the strong Lewis acid sites, so that the hydrolysis-dehydroxylation cycle, which might proceed on strong Lewis acid sites, is greatly suppressed.

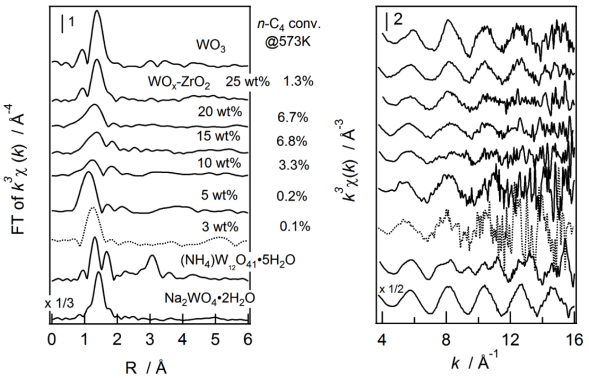

Fig. 6 W K-edge EXAFS Spectra and Fourier Transforms of WO_x–ZrO_2 Catalysts and Reference Compounds

2. 2. Tungsten–zirconium Oxides[21)]

Since Hino and Arata have developed zirconium oxide supported tungsten-oxide (WZ; WO_x–ZrO_2) catalysts promote *n*-butane isomerization even at ambient temperatures[22),23)], such WZ catalysts are very interesting because of the remarkable strong acidity, high thermal stability up to 1100 K, easy preparation procedures and handling, and anomalous acidity generation mechanisms[21),24)~27)]. The activity is strongly dependent on the loading amounts and calcination temperature. The appropriate preparation condition is WO_3-loading of 15-20 wt% and calcination temperature of 1073 K. The loading amounts correspond to the values of the theoretical monolayer of WO_x species on the surface of ZrO_2. Various structures of the active sites have been proposed[24)~29)]; but remain incompletely understood. W L_3-edge EXAFS and L_1-edge XANES characterization by Barton *et al.* indicated that WO_x species have a distorted octahedral symmetry with a static disorder similar to that in bulk WO_3[28)]. However, RSFs failed to clearly show the second coordination spheres around tungsten. Zr-based compounds usually contain Hf impurities, so that W L_3-edge EXAFS (10.2 keV) of a tungsten–zirconium binary phase is available for a narrow *k*-range of less than ~11 $Å^{-1}$ due to interference by the Hf L_2-edge (10.7 keV). The narrow utilization range would lead to absence of contributions from heavy elements (W–W and/or W–Zr pairs) to the EXAFS due to their characteristic dependences of back scattering amplitudes on *k*[30)]. Therefore, we tried to characterize active tungsten species in WZ by W K-edge (69.5 keV) EXAFS and L_1-edge XANES techniques[21)].

Figure 6 shows the W K-edge EXAFS spectra of WZ samples with different loadings and their Fourier transforms in the ranges of 4-14 $Å^{-1}$. With WO_3 loadings of less than 5 wt% (catalytically inactive for *n*-butane skeletal isomerization), only a single peak was

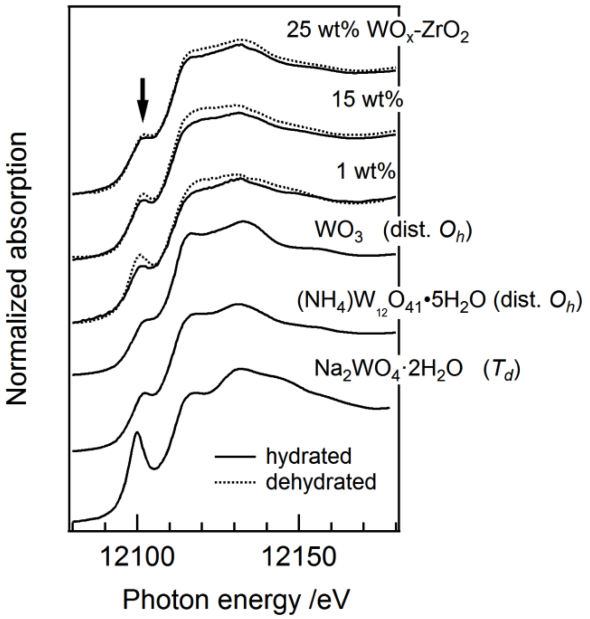

Fig. 7 W L_1-edge XANES Spectra of WO_x–ZrO_2 Catalysts in Dried and Hydrated States

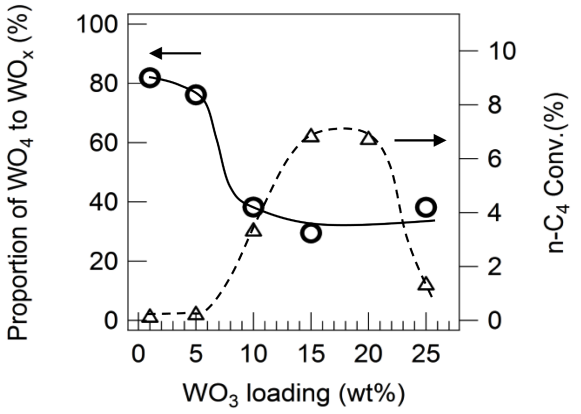

Catalyst: 200 mg, *n*-butane: 150 μmol, 573 K, 24 h.

Fig. 8 Dependence of Loading Amounts of WO_x Species on Proportion of WO_4 Species in WO_x–ZrO_2 and Catalytic Activity for *n*-Butane Skeletal Isomerization

observed around 1.2 Å in the RSFs. The peak intensities for 10-20 wt% WZ (active catalyst) were weaker than those for 5 wt% WZ, indicating that structural ordering for W–O pairs were lowered due to their large Debye-Waller factors. The RSF for 25 wt% WO_3 was almost identical to that of WO_3 crystal. The phase diagram for the WO_3–ZrO_2 system[31] indicates that 2.5 mol% WO_3 would be dissolved into ZrO_2 to form a solid solution. It is possible that a part of the tungsten forms a solid solution during the catalyst preparation step, as for Fe- and Mn-promoted sulfated zirconia[32]. No second coordination sphere was observed around 3 Å in the RSF of WZ samples. Consequently the second coordination environment could not be analyzed even with W K-edge EXAFS.

The spectral configuration in the pre-edge region of W L_1-edge XANES spectra is sensitive to the symmetry of tungsten species because the 2*s* electron could transition to *p*-orbitals *via* an intense electric dipole process or to *d*-orbitals *via* a weak electric quadrupole process[33),34]. An intense pre-edge peak could be observed for a compound with tetrahedral WO_4, but only a tiny peak would be observable for the symmetrical WO_x unit. **Figure 7** shows the W L_1-edge XANES spectra of reference compounds and WZ in the hydrated or dried state. The pre-edge peak of Na_2WO_4 (tetrahedron) around 12,100 eV is much more intense than those of WO_3 and ammonium–paratungstate (distorted octahedron). The pre-edge peak intensities for all WZ samples in the hydrated state were almost identical, and slightly larger than that for WO_3. The pre-edge peak intensity of WZ with 1 wt%-loadings was much greater in the dried state than in the hydrated state. Differences in the pre-edge peak intensity between the dried and hydrated states were not remarkable at high loadings of 25 wt%. Incremental increase of pre-edge peak intensity during dehydration has been reported in some cases such as VO_x/SiO_2[35),36)] and WO_x/Al_2O_3[37)]. These phenomena could be considered as the changing symmetry of the coordination environment caused by elimination of adsorbed H_2O molecules from MO_4 species. Similarly, the changes in pre-edge peak intensities shown in **Fig. 7** could be interpreted as WO_4 and/or WO_5 polyhedral species in the dehydrated state transforming to WO_6-like species by adsorbing water molecules, and the fraction of WO_6 species in a dried state varied with the tungsten loading. The estimated ratios of WO_4 to all WO_x polyhedrons based on the behavior of the pre-edge peaks are shown in **Fig. 8**. Catalytic activities for *n*-butane skeletal isomerization are also plotted in **Fig. 8** as a function of WO_x loadings. With tungsten loading of 5 wt% or less, W species on inert catalyst was present mainly as tetrahedrons. With higher loadings, most W species were present as WO_6.

Based on XRD and W K- and L-edge characterization and the phase diagram of WO_3–ZrO_2 system, we proposed that tungsten species present on active WO_x–ZrO_2 catalyst with 15 wt% loading consist of a mixture of WO_3–ZrO_2 solid solution, WO_6 aggregates (WO_x cluster) and WO_4 species on the surface. Possible structures of WZ at different loadings are shown in **Fig. 9**. WO_6 aggregates on the surface of the tetragonal ZrO_2-based phase are proposed to be active species with similar symmetry to that of WO_3 crystal, although the exact local structure and the two- or three-dimensional network remain unclear. Recently, Kitano and their research group reported that two-dimensional tungsten oxide monolayer on Al_2O_3 calcined at 1123 K

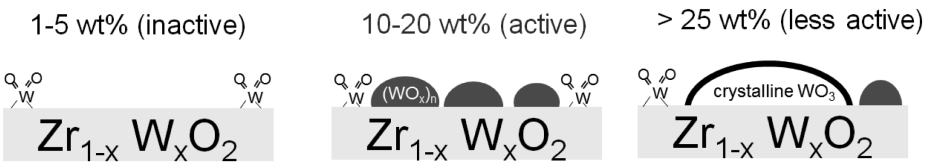

Fig. 9 Possible Structures of WO_x–ZrO_2 with Different Loadings

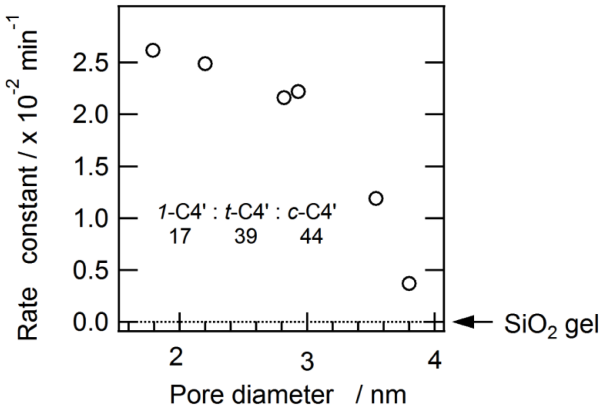

Catalyst: 50 mg, 2-buthanol: 150 µmol, 423 K.

Fig. 10 Pore Size Dependence of Activity of 2-Butanol Dehydration on Mesoporous Silica FSM-16

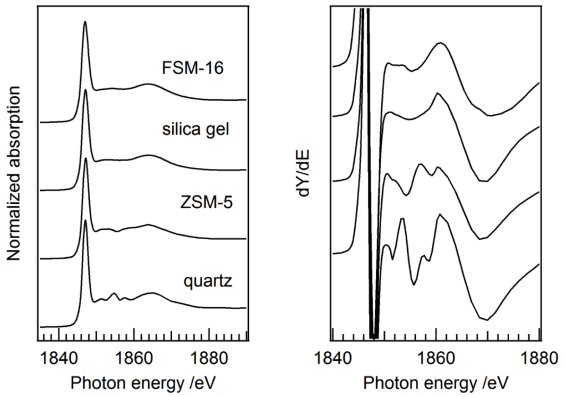

Fig. 11 Si K-edge XANES Spectra and First Derivatives of Silica Based Samples

have strong Brønsted acidity[38]. Hydroxyl groups on boundaries between the WO_3 monolayer domains were proposed to act as the acid sites. Possibly similar acid-species would be formed on the surface of 10-20 wt% WO_3–ZrO_2 calcined at 1073 K, with the surface concentration corresponding to the theoretical monolayer.

2. 3. Hexagonally Ordered Mesoporous Silica[39]

Amorphous silica is known to be catalytically inert because of the weak acidity of silanol groups. However, siliceous hexagonally ordered mesoporous silicas such as FSM-16[40)~44)] and MCM-41[45)~49)] were found to show catalytic activity several years after the first description of mesoporous silicas[50)~52)]. We independently found that siliceous mesoporous silica FSM-16 promoted some acid catalyzed reactions, and have been investigating the acidic properties of FSM-16. We proposed that weakly perturbed silanol groups on the surface of the specific hexagonally ordered pore structure with thin wall act as Brønsted acid sites, with medium strength of $H_0 = -3.0$[41)], and strained siloxane bridges formed by dehydration of isolated silanol groups act as the Lewis acid site[42)]. The catalytic activity for 2-butanol dehydration was found to depend on pore size of FSM-16 in the range of 1.8 to 3.8 nm (**Fig. 10**)[44)] as for acetalization by MCM-41[49)]. We have also confirmed that amorphous silicas prepared from the same raw materials as the active FSM-16 were inactive, and collapsed FSM-16 without ordered porosity was as well. We assume that the acidic property of FSM-16 originates from the characteristic ordered pore structure with thin walls[52),53)] that permits the existence of strained siloxane bridges, which would induce Brønsted acidity in the silanol groups. To confirm the presence of the strained pore structure and verify our acidity generation hypothesis of siliceous mesoporous silicas, the coordination environments of Si species in various types of silicas were investigated by Si–K edge X-ray absorption spectroscopic techniques[39)].

Figure 11 shows the Si K-edge XANES spectra of silica materials and the first derivatives. All XANES spectra exhibited a strong whiteline around 1847 eV which is assigned to transition of the 1*s* electron to the 3*p* orbital in SiO_4 tetrahedral species[54),55)]. The configurations of all spectra and the apparent absorption edges were quite similar to those of amorphous silica. Fine peaks around 1850-60 eV appeared on the XANES spectra of crystalline quartz and microporous crystal ZSM-5, but not for FSMs and amorphous silicas. The absence of such fine peaks indicates that silicon species in FSM-16s are present as SiO_4 species without long-range ordering. This finding is consistent with the pioneering ^{29}Si NMR and Raman study for MCM-41[56)] showing the amorphous wall structure of mesoporous silicas. This interpretation of XANES; *i.e.* absent long-range ordering of the structure inside the pore wall of FSM-16, was supported by theoretical calculations for silicas by Wu *et al.*[55)]. They reported that the fine peaks observed in the experimental XANES spectrum of crystalline silica could be reproduced by calculation

using the 109-atom cluster, but are absent using the 5-atom cluster.

To investigate the local structure around the silicon atom in more detail, Si K-edge EXAFS analyses were performed. **Figure 12** shows the k^3-weighted EXAFS spectra of silica samples and their Fourier transforms (RSFs: radial structure functions). All other spectra of the mesoporous samples, ZSM-5 and silica gel had very similar configurations except for a tiny shoulder around 7 $Å^{-1}$ confirmed on mesoporous samples. The complicated configuration of the EXAFS spectrum of quartz indicates that the EXAFS function consists of at least two curves with different frequencies. The second coordination sphere was confirmed in the RSF of quartz around 2.4 Å due to Si–(O)–Si pairs. However, this was not distinct because the scattering atom is the light element silicon and the *k*-range of the Fourier transformation was as short as *ca.* 3-9 $Å^{-1}$. It is well known that the size of the siloxane ring in amorphous silica is distributed. Therefore, the larger static disorder for Si–Si in other silica materials, *i.e.* Si–Si bond length is not uniform, unfortunately prevented EXAFS analysis of Si–(O)–Si pairs for amorphous and mesoporous silicas.

Curve fitting analysis for the first coordination sphere was performed to compare the averaged interatomic distances of SiO_4 units for both k^1- and k^3-weighted EXAFS. Curve-fitting analyses were then carried out with fixed parameters of coordination number (4) and energy of the apparent absorption edge to clarify very faint structural differences between the various silica samples. The curve fitting analyses for the first coordination sphere revealed that no systematic changes in Si–O bond length with pore diameter could be confirmed. However, **Table 1** shows that averaged bond lengths for all mesoporous silicas were slightly longer than that of amorphous silica by *ca.* 0.02 Å. Based on the EXAFS analysis, we propose that this slightly longer Si–O interatomic distance for FSM compared to amorphous silica is evidence of the strained pore wall structure. The strained siloxane bridge would result in partial enlargement of the Si–O bridge. The elongated Si–O bond could be regarded as a pseudo-coordinative unsaturated silicon species which acts as a Lewis acid site, as similar cases which have been predicted by theoretical calculations by Kawakami and Yoshida[57)~59)]. Our proposal for the acidity generation mechanism of siliceous mesoporous silica is based on strained siloxane structures related to the ordered meso-porosity with thin walls[42)]. The present EXAFS analysis does not compete with our proposal that strained SiO_4 species intrinsically exist inside the pore walls as illustrated in **Fig. 13**. The dependence of Si–O bond length on the pore size was not consistent with that of catalytic activity as mentioned above. As the evaluated bond lengths were averaged for all Si–O bonds including the silanol groups, further investigations to clarify the exact length and the fraction of the strained sites are required.

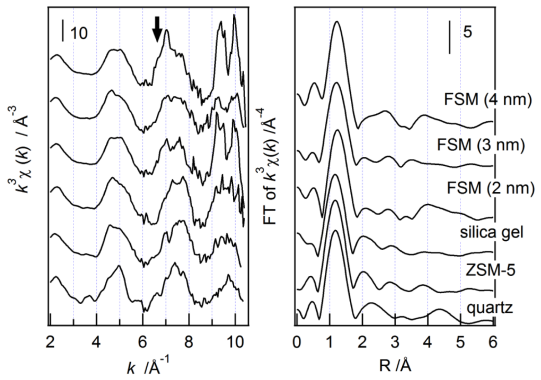

Fig. 12 Si K-edge EXAFS Spectra and Fourier Transforms of Silica Based Samples

3. Remarks on the EXAFS Analysis

3. 1. Possibility of Coexistence of Multiple Phases

The usual EXAFS spectrum reflects averaged structural information around the target element. Interpretation of evaluated EXAFS parameters requires great care, especially for heterogeneous catalysts which sometimes contain several chemical species and/or dif-

Table 1 Results of the Curve Fitting Analysis of Silica Samples for the First Coordination Sphere

Sample	a_0 [Å]	d_{BJH}[a)] [Å]	S_{BET}[b)] [m^2/g]	k^1			k^3		
				r [Å]	σ^2 [Å$^2\times$1000]	R[c)] [%]	r [Å]	σ^2 [Å$^2\times$1000]	R[c)] [%]
quartz				1.610 ± 0.009	3.0 ± 0.8	5.1	1.609 ± 0.008	3.5 ± 0.8	0.6
ZSM-5				1.598 ± 0.009	2.9 ± 0.8	4.9	1.594 ± 0.008	3.5 ± 0.4	0.7
SiO_2 gel (1)		-	200	1.595 ± 0.009	2.2 ± 1.1	2.9	1.594 ± 0.007	2.4 ± 0.6	1.1
SiO_2 gel (2)				1.601 ± 0.010	4.9 ± 0.6	7.6	1.599 ± 0.008	5.3 ± 0.3	0.9
FSM (2 nm)	41.4	21	780	1.611 ± 0.009	3.2 ± 0.7	2.3	1.617 ± 0.007	3.7 ± 0.4	1.4
FSM (3 nm)	41.4	28	990	1.619 ± 0.009	3.4 ± 0.7	4	1.619 ± 0.008	4.2 ± 0.3	0.6
FSM (4 nm)	59.3	36	875	1.625 ± 0.009	2.1 ± 1.0	0.7	1.632 ± 0.007	1.6 ± 0.7	1.3

a) BJH pore diameter.
b) BET specific surface area.
c) $R = \sum\left(k^n\chi_{obs} - k^n\chi_{calc}\right)^2 \Big/ \sum\left(k^n\chi_{obs}\right)^2 \times 100.$

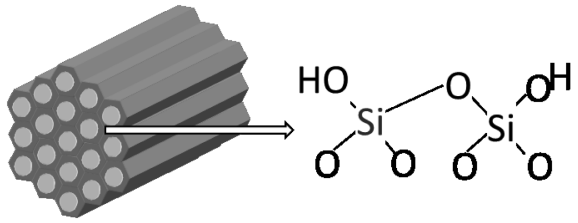

Fig. 13 Possible Structure of Strained Silicon Species within the Thin Pore Wall of Mesoporous Silica

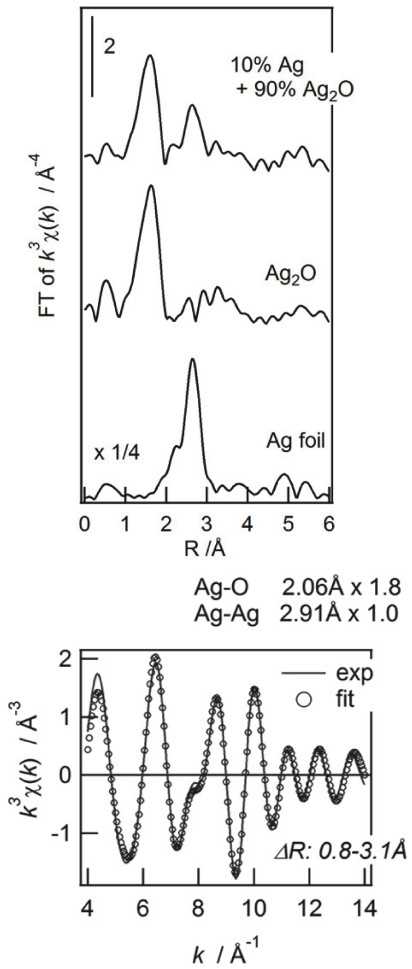

The simulated spectrum consists of 10 % metallic Ag and 90 % Ag_2O.

Fig. 14 Radial Structure Functions of Ag K-edge EXAFS for Ag Powder, Ag_2O and Simulated Mixture, and the Result of Curve-fitting Analysis

ferent domain sizes. We demonstrate a model case which contains both metallic and oxide species. **Figure 14** shows the Fourier transform Ag K-edge EXAFS spectra of Ag foil, Ag_2O and simulated spectra of the metallic Ag and Ag_2O mixture with atomic ratio 1 : 9. The RSF of the model spectrum shows two peaks at 1.6 Å and 2.6 Å, and curve-fitting analysis of the inverse Fourier transform EXAFS has a satisfactory

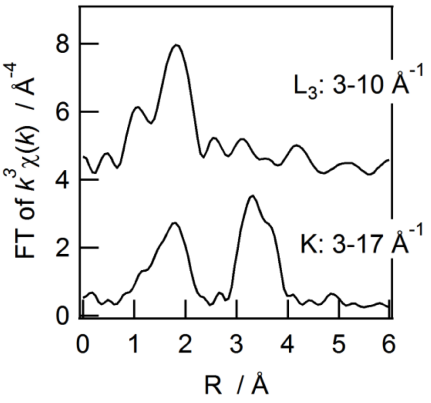

Fig. 15 Fourier Transforms of Ce L_3- and K-edge EXAFS Spectra of the Same $Ce_{0.5}Zr_{0.5}O_2$ Sample

fit with a two shell model (Ag–O: 2.06 Å × 1.8; Ag–Ag: 2.91 Å × 1.0). Such evaluated EXAFS parameters might indicate incorrect structural models such as a diatomic complex. The reliability of interpretations would be improved by considering the evaluated interatomic distances. The interatomic distance of the Ag–Ag pair in fcc-type metallic silver is 2.89 Å with coordination number 12. If a silver cluster consists of several atoms, the interatomic distance should be generally much shorter than in the large fcc-type particles due to less steric hindrance. In fact, the interatomic distances of the silver cluster in zeolites[60),61)] or on Al_2O_3[62),63)] were reported as 2.74-2.84 Å. Interpretation of the analyzed Ag-Ag pairs with evaluated bond-length of 2.91 Å and low coordination number suggests that a part of large metallic Ag particles are also present.

3. 2. Mismatch between Radial Distribution Function and Fourier Transform EXAFS

The Fourier transform EXAFS spectrum does not always reflect the radial distribution function (RDF). EXAFS characterizations for 6th period elements are usually performed at the L_3 edges. For light rare earth elements such as La and Ce, the available *k*-region of the EXAFS is limited up to 10 $Å^{-1}$ due to the presence of the L_2 edge. EXAFS analyses with narrow ranges would reduce the accuracy. A typical example of this discrepancy can be seen in the analysis of the Ce site in CeO_2–ZrO_2 automobile co-catalyst. **Figure 15** shows Fourier transform k^3-weighted Ce K- and L_3-edge EXAFS (RSFs) of $Ce_{0.5}Zr_{0.5}O_2$ automobile co-catalyst[64)]. A distinct peak is observed around 3-4 Å in the RSF of the Ce K-edge, but was absent for the Ce L_3-edge EXAFS. Ce K-edge EXAFS and XRD characterizations have revealed that the $Ce_{0.5}Zr_{0.5}O_2$ sample forms a highly crystallized solid solution homogeneously dispersed at the atomic level[64)]; but the corresponding Ce L_3-edge EXAFS characterization might incorrectly suggest that Ce-species are present in a highly dispersed form or the sample was X-ray amorphous. Absence of

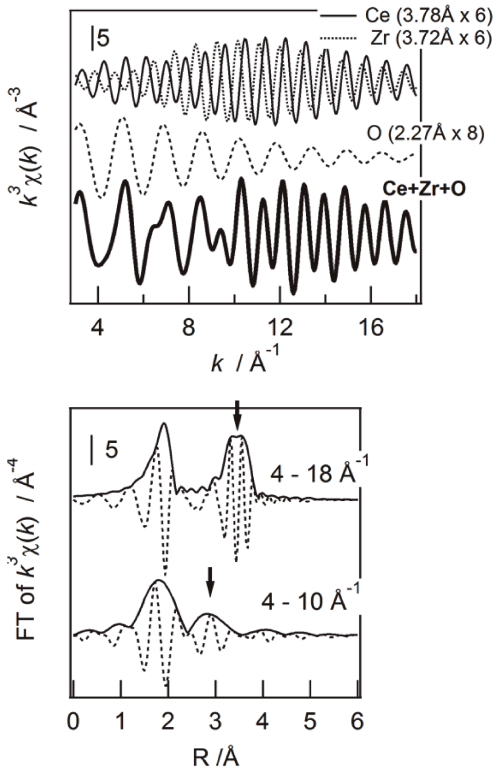

The Fourier transforms do not reflect the true radial distribution function around Ce.

Fig. 16 Simulated Ce K-edge EXAFS Spectra of $Ce_{0.5}Zr_{0.5}O_2$ for Ce–Zr, Ce–Zr, Ce–O Pairs and the Sum, and the Fourier Transforms with Different *k*-Ranges

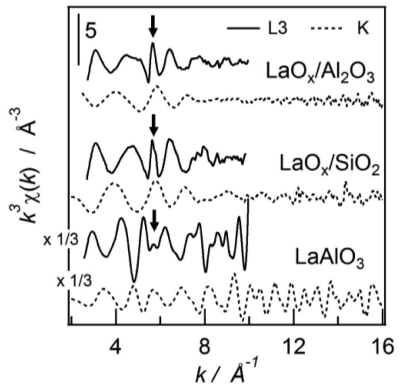

The spike indicated by arrows in the L_3-edge EXAFS was due to multi-electron excitations which should be ignored for structural characterization.

Fig. 17 Comparison of La K- and L_3-edge EXAFS Spectra of Supported Lanthanum Oxide

the second coordination sphere at the Ce L_3 edge was caused by interference to the EXAFS signals. As easily checked with theoretical tables[65], the phase shifts of Zr and Ce scatters differ by almost π radian. Therefore, these two EXAFS oscillations with identical interatomic distances are inverse, resulting in drastic reduction of the amplitude of the total EXAFS function. This finding could be clearly confirmed by simulation of the EXAFS function for the model structure. **Figure 16** shows the simulated Ce K-edge EXAFS spectra of each scatterer with the same structural parameters as for **Fig. 15**. Clearly the phase of the EXAFS oscillation for the Ce–Ce pair is completely inverse to that of the Ce–Zr pair especially in the 4-10 Å^{-1} regions. As a result, the Fourier transforms of the simulated Ce K-edge EXAFS with narrow *k*-range could not reflect the actual radial distributions. Furthermore, we would like to emphasize that the peak position and the intensity of the second coordination sphere for simulated EXAFS remarkably differed according to the *k*-range utilized. It clearly shows that the peak position of the RSF does not always reflect the interatomic distance or confirm the existence of bonds unless the coordination shell consists of a single component with the same interatomic distance. To avoid such mistaken interpretations, it is important that the range of Fourier transforms should be long as possible, and the configuration of the RSF should be checked with various *k*-ranges and *k*-weights. The degree of cancellation of EXAFS oscillation based on differences in each phase shift would be remarkable if the pair of scattering atoms was O and Cl, or O and S, for example.

3. 3. Effects of Multiple Excitations

Multi-electron excitation phenomena are sometimes observed especially in L_3-edge EXAFS for lanthanide compounds[7),66)~68)], which would complicate structural analyses. **Figure 17** shows the La K- and L_3-edge EXAFS spectra of crystalline $LaAlO_3$ and X-ray amorphous supported lanthanum oxides[7)]. The distinct spike due to multi-electron excitation from $2p4d$ to $(5d)^2$ was clearly observed in each L_3 edge EXAFS spectra at around 5.6 Å^{-1}. The intensities are obviously ignorable compared with the amplitudes of true EXAFS oscillations, indicating that reliable EXAFS analyses are virtually impossible at the La L_3 edge. In contrast to the La L_3 edge, no spikes due to multi-electron excitations were observed in the K-edge EXAFS. The available *k*-ranges are considerably wider. Therefore, characterization with *Ln* K-edge XAFS instead of L_3-edge XAFS is very important to obtain detailed structural information.

4. Summary

This review paper presents XAFS studies of solid acid-base catalysts utilized for structural characterizations and/or interpretations for physical properties. X-ray absorption spectroscopy is widely used in the fields of catalysts and catalysis for characterization. Successive development of measurement facilities,

instruments and equipment, and analytical techniques as well as performance of personal computers has been remarkable. Recent developed highly time- or specially resolved, and *in-situ* XAFS techniques have also clarified novel concepts and new phenomena which could not be observed previously. Number of recorded X-ray absorption spectra for once experimental machine-time has been increasing dramatically in recent days, so the author is concerned about the situation that careless or automatic analyses of too much spectra may give correct conclusions. It has been usually pointed out that EXAFS parameters obtained by a curve-fitting analysis include errors. Correlation of each EXAFS parameters and maximum number of parameters has been noted as well. Again, interpretation of XAFS should be done carefully. The present review emphasized some other problems for EXAFS analysis which have not been often pointed out.

References

1) Sayers, D. E., Stern, E. A., Lytle, F. W., *Phys. Rev. Lett.*, **27**, 1204 (1971).
2) Lytle, F. W., *J. Synchrot. Radiat.*, **6**, 123 (1999).
3) Bart, J. C. J., *Adv. Catal.*, **34**, 203 (1986).
4) Iwasawa, Y., "X-Ray Absorption Fine Structure for Catalysts and Surfaces," World Scientific, Singapore (1996).
5) Clausen, B. S., Topsøe, H., Frahm, R., *Adv. Catal.*, **42**, 315 (1998).
6) Bare, S. R., Ressler, T., *Adv. Catal.*, **52**, 339 (2009).
7) Yamamoto, T., Tanaka, T., Matsuyama, T., Funabiki, T., Yoshida, S., *J. Synchrot. Radiat.*, **8**, 634 (2001).
8) Yamamoto, T., Hatsui, T., Matsuyama, T., Tanaka, T., Funabiki, T., *Chem. Mat.*, **15**, 4830 (2003).
9) Tanabe, K., Holderich, W. F., *Appl. Catal. A: General*, **181**, 399 (1999).
10) Schaper, H., Doesburg, E. B. M., van Reijen, L. L., *Appl. Catal.*, **7**, 211 (1983).
11) Oudet, F., Courtine, P., Vejux, A., *J. Catal.*, **114**, 112 (1988).
12) Beguin, B., Garbowski, E., Primet, M., *Appl. Catal.*, **75**, 119 (1991).
13) Ozawa, M., Kimura, M., Isogai, A., *J. Mater. Sci.*, **26**, 4818 (1991).
14) Church, J. S., Cant, N. W., Trimm, D. L., *Appl. Catal. A: General*, **107**, 267 (1994).
15) Loong, C. K., Richardson, J. W., Ozawa, M., *J. Alloy. Compd.*, **250**, 356 (1997).
16) Haack, L. P., de Vries, J. E., Otto, K., Chattha, M. S., *Appl. Catal. A: General*, **82**, 199 (1992).
17) Chen, X. Y., Liu, Y., Niu, G. X., Yang, Z. X., Bian, M. Y., He, A., *Appl. Catal. A: General*, **205**, 159 (2001).
18) Rossignol, S., Kappenstein, C., *Int. J. Inorg. Mater.*, **3**, 51 (2001).
19) Yamamoto, T., Tanaka, T., Suzuki, S., Kuma, R., Teramura, K., Kou, Y., Funabiki, T., Yoshida, S., *Topic. Catal.*, **18**, 113 (2002).
20) Yamamoto, T., Tanaka, T., Matsuyama, T., Funabiki, T., Yoshida, S., *J. Phys. Chem. B*, **105**, 1908 (2001).
21) Yamamoto, T., Orita, A., Tanaka, T., *X-Ray Spectrom.*, **37**, 226 (2008).
22) Hino, M., Arata, K., *J. Chem. Soc., Chem. Commun.*, 1259 (1988).
23) Arata, K., Hino, M., *Proc. 9th Intern. Congr. Catal.*, **4**, 1727 (1989).
24) Arata, K., *Appl. Catal. A: General*, **146**, 3 (1996).
25) Scheithauer, M., Grasselli, R. K., Knozinger, H., *Langmuir*, **14**, 3019 (1998).
26) Barton, D. G., Shtein, M., Wilson, R. D., Soled, S. L., Iglesia, E., *J. Phys. Chem. B*, **103**, 630 (1999).
27) Zhou, W., Ross-Medgaarden, E. I., Knowles, W. V., Wong, M. S., Wachs, I. E., Kiely, C. J., *Nature Chem.*, **1**, 722 (2009).
28) Barton, D. G., Soled, S. L., Meitzner, G. D., Fuentes, G. A., Iglesia, E., *J. Catal.*, **181**, 57 (1999).
29) Naito, N., Katada, N., Niwa, M., *J. Phys. Chem. B*, **103**, 7206 (1999).
30) Teo, B. K., "EXAFS: Basic Principles and Data Analysis," Springer-Verlag, Berlin (1986).
31) Chang, L. L. Y., Scroger, M. G., Phillips, B., *J. Am. Ceram. Soc.*, **50**, 211 (1967).
32) Yamamoto, T., Tanaka, T., Takenaka, S., Yoshida, S., Onari, T., Takahashi, Y., Kosaka, T., Hasegawa, S., Kudo, M., *J. Phys. Chem. B*, **103**, 2385 (1999).
33) Yamamoto, T., *X-Ray Spectrom.*, **37**, 572 (2008).
34) Yamazoe, S., Hitomi, Y., Shishido, T., Tanaka, T., *J. Phys. Chem. C*, **112**, 6869 (2008).
35) Yoshida, S., Tanaka, T., Nishimura, Y., Mizutani, H., Funabiki, T., *Proc. 9th Intern. Congr. Catal.*, **3**, 1473 (1989).
36) Gao, X. T., Bare, S. R., Weckhuysen, B. M., Wachs, I. E., *J. Phys. Chem. B*, **102**, 10842 (1998).
37) Horsley, J. A., Wachs, I. E., Brown, J. M., Via, G. H., Hardcastle, F. D., *J. Phys. Chem.*, **91**, 4014 (1987).
38) Kitano, T., Hayashi, T., Uesaka, T., Shishido, T., Teramura, K., Tanaka, T., *ChemCatChem*, **6**, 2011 (2014).
39) Yamamoto, T., Mori, S., Kawaguchi, T., Tanaka, T., Nakanishi, K., Ohta, T., Kawai, J., *J. Phys. Chem. C*, **112**, 328 (2008).
40) Nakajima, T., Nakajima, T., Mishima, S., *Nippon Kagaku Kaishi*, 565 (1997).
41) Yamamoto, T., Tanaka, T., Funabiki, T., Yoshida, S., *J. Phys. Chem. B*, **102**, 5830 (1998).
42) Yamamoto, T., Tanaka, T., Inagaki, S., Funabiki, T., Yoshida, S., *J. Phys. Chem. B*, **103**, 6450 (1999).
43) Shouro, D., Moriya, Y., Nakajima, T., Mishima, S., *Appl. Catal. A: General*, **198**, 275 (2000).
44) Yamamoto, T., Mori, S., Shishido, T., Kawai, J., Tanaka, T., *Top. Catal.*, **52**, 657 (2009).
45) Hartmann, M., Poppl, A., Kevan, L., *J. Phys. Chem.*, **99**, 17494 (1995).
46) Galarneau, A., Barodawalla, A., Pinnavaia, T. J., *Chem. Commun.*, 1661 (1997).
47) Tanaka, Y., Sawamura, N., Iwamoto, M., *Tetrahedron Lett.*, **39**, 9457 (1998).
48) Ishitani, H., Iwamoto, M., *Tetrahedron Lett.*, **44**, 299 (2003).
49) Iwamoto, M., Tanaka, Y., Sawamura, N., Namba, S., *J. Am. Chem. Soc.*, **125**, 13032 (2003).
50) Yanagisawa, T., Shimizu, T., Kuroda, K., Kato, C., *Bull. Chem. Soc. Jpn.*, **63**, 988 (1990).
51) Kresge, C. T., Leonowicz, M. E., Roth, W. J., Vartuli, J. C., Beck, J. S., *Nature*, **359**, 710 (1992).
52) Inagaki, S., Fukushima, Y., Kuroda, K., *J. Chem. Soc., Chem. Commun.*, 680 (1993).
53) Inagaki, S., Koiwai, A., Suzuki, N., Fukushima, Y., Kuroda, K., *Bull. Chem. Soc. Jpn.*, **69**, 1449 (1996).
54) Lermer, H., Draeger, M., Steffen, J., Unger, K. K., *Zeolites*, **5**, 131 (1985).
55) Wu, Z. Y., Jollet, F., Seifert, F., *J. Phys., Cond. Matter.*, **10**, 8083 (1998).
56) Chen, C. Y., Li, H. X., Davis, M. E., *Microporous Mater.*, **2**, 17 (1993).
57) Kawakami, H., Yoshida, S., Yonezawa, T., *J. Chem. Soc., Faraday Trans. II*, **80**, 205 (1984).
58) Yoshida, S., Kawakami, H., "Acid-Base Catalysis," eds. by

Tanabe, K., Hattori, H., Yamaguchi, T., Tanaka, T., Kodansha, Tokyo (1989), p. 123.
59) Yoshida, S., *Hyomen Kagaku*, **11**, 390 (1990).
60) Shibata, J., Takada, Y., Shichi, A., Satokawa, S., Satsuma, A., Hattori, T., *J. Catal.*, **222**, 368 (2004).
61) Yamamoto, T., Takenaka, S., Tanaka, T., Baba, T., *J. Phys.: Conf. Ser.*, **190**, 1417075 (2009).
62) Shimizu, K., Satsuma, A., *J. Jpn. Petrol. Inst.*, **54**, (6), 347 (2011).
63) Shimizu, K., Tsuzuki, M., Kato, K., Yokota, S., Okumura, K., Satsuma, A., *J. Phys. Chem. C*, **111**, 950 (2007).
64) Nagai, Y., Yamamoto, T., Tanaka, T., Yoshida, S., Nonaka, T., Okamoto, T., Suda, A., Sugiura, M., *Catal. Today*, **74**, 225 (2002).
65) Teo, B. K., Lee, P. A., *J. Am. Chem. Soc.*, **101**, 2815 (1979).
66) Chaboy, J., Marcelli, A., Tyson, T. A., *Phys. Rev. B*, **49**, 11652 (1994).
67) Solera, J. A., Garcia, J., Proietti, M. G., *Phys. Rev. B*, **51**, 2678 (1995).
68) Ohta, A., Kagi, H., Tsuno, H., Nomura, M., Kawabe, I., *Am. Miner.*, **93**, 1384 (2008).

……

要　　旨

X 線吸収分光法を用いた固体酸塩基触媒の評価

山本　　孝

徳島大学大学院総合科学教育部，770-8502 徳島市南常三島町1-1

X 線吸収分光法により固体酸塩基触媒の構造解析および物性評価手法として利用した研究例を紹介した。アルミナの熱耐久性を向上させる効果があるランタンイオンについて，シンタリング抑制効果が発現する低添加量でもランタン種はペロブスカイト相を形成せずに孤立高分散状態で存在することを示した。固体強酸触媒タングステン–ジルコニウム酸化物触媒のタングステン種の存在状態について論じた。メソポーラスシリカが固体酸性質を発現することについて，歪んだシロキサン結合が薄い細孔壁中に存在することを示した。また，EXAFS 解析に際して誤った結論を導きかねない事例について，構造の異なる複数の成分が共存する可能性の考察，EXAFS 関数のフーリエ変換が動径構造関数を反映しない実例とその要因，多電子励起の影響について解説した。

……